

Supporting Information for:

Chiral Coordination Polymers Based on d^{10} metals and 2-aminonicotinate with Blue Fluorescent/Green Phosphorescent Anisotropic Emissions

Oier Pajuelo-Corral,^a Antonio Rodríguez-Diéguez,^b Jose A. García,^c Eider San Sebastián,^a Jose M. Seco,^{*a} and Javier Cepeda^{*a}

^a Departamento de Química Aplicada, Facultad de Química, Universidad del País Vasco (UPV/EHU), 20018 Donostia, Spain. ^b Departamento de Química Inorgánica, Facultad de Ciencias, Universidad de Granada, 18071 Granada, Spain. ^c Departamento de Física Aplicada, Facultad de Ciencia y Tecnología, Universidad del País Vasco (UPV/EHU), 48940 Leioa, Spain.

Contents:

- S1. Powder X-ray Data Collection.
- S2. Structural details of compound **1**.
- S3. FT-IR spectroscopy.
- S4. Thermogravimetric results for compound **2**.
- S5. Photoluminescence measurements.
- S6. Lifetime measurements.
- S7. TD-DFT computational details.
- S8. Calculation of the lowest-lying triplet state (T_1).
- S9. Time-resolved emission spectra.

S1. Powder X-ray Data Collection.

Table S1 and Figure S1 summarize the data resulting from the PXRD pattern-matching analyses performed on compounds **1** and **2**, which confirm the purity of these samples.

Table S1. PXRD pattern-matching results of compound **1** and **2**.

	1	2
Empirical formula	C ₁₂ H ₁₀ N ₄ O ₄ Zn	C ₁₂ H ₁₀ CdN ₄ O ₄
Formula weight	339.62	386.64
Crystal system	Tetragonal	Tetragonal
Space group	<i>P4₃2₁2</i>	<i>P4₃2₁2</i>
<i>a</i> (Å)	7.952(3)	8.154(2)
<i>b</i> (Å)	7.952(3)	8.154(2)
<i>c</i> (Å)	19.941(6)	20.052(4)
V (Å ³)	1260.7(7)	1333.3(6)
Z	4	4
ρ (g cm ⁻³) (calcd. / exp.)	1.79 / 1.80 (1)	1.93 / 1.94(1)
Chi ²	1.94	2.94

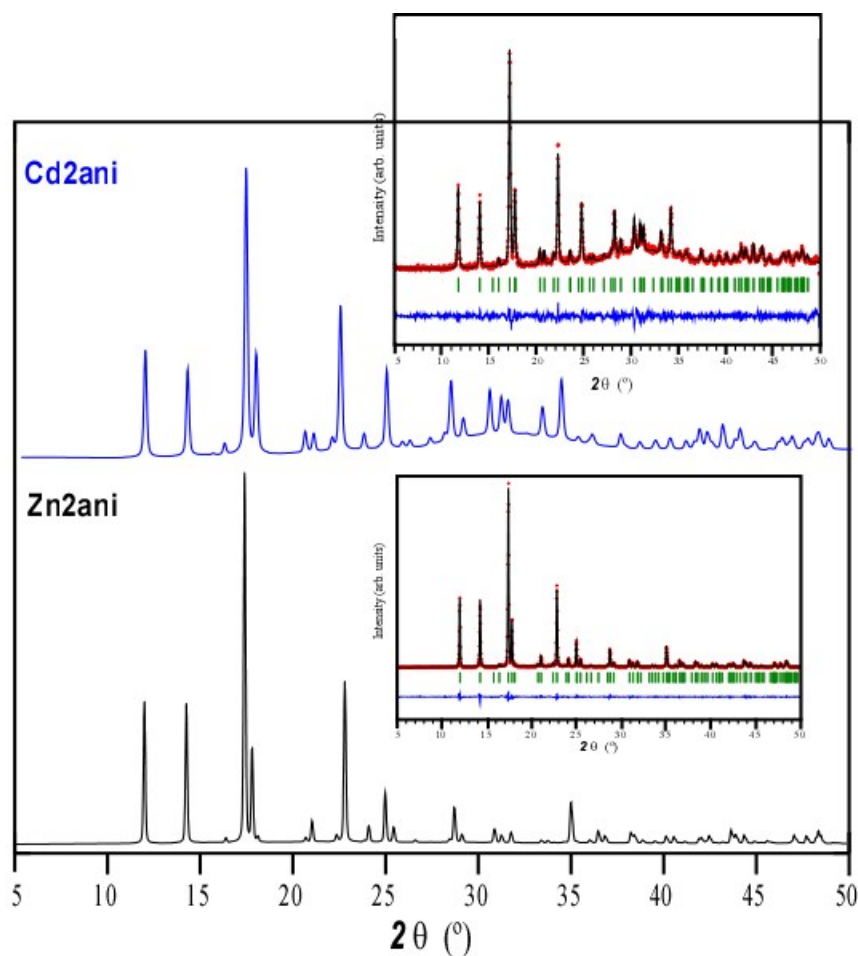


Figure S1. Comparison of experimental diffractogram of **2** and the theoretical one of **1** with their full profile pattern-matching analyses.

S2. Structural details of compound 1.

Table S2. Structural parameters (Å, °) of hydrogen bonds (Å, °) in compound 1.^a

$D-H\cdots A^b$	$D-H$	$H\cdots A$	$D\cdots A$	$D-H\cdots A$
N21–H21a \cdots O2(iv)	0.86	2.10	2.906(6)	155.7
N21–H21b \cdots O1	1.02	2.37	3.096	127.4

^a Symmetry codes: (iv) $-y + 2, -x + 1, -z + 1/2$. ^b D: donor. A: acceptor.

Table S3. Structural parameters (Å, °) of π – π interactions of compound 1.^a

Ring \cdots Ring ^b	α	DC	β	DZ	Dist.
1A–1A(v)	37.93	4.235(3)	38.27	4.20	3.43–5.07
1A–1A(vi)	78.84	4.961(2)	44.92	3.52	3.43–5.07

[a] Symmetry: (v) $-y - 1, -x + 2, -z + 1/2$; (vi) $-y + 3/2, x + 3/2, z + 3/4$. α : dihedral angle between mean planes of the rings (°), DC: distance between ring centroids (Å), β : angle between DC vector and normal to plane(I) (°), DZ: perpendicular distance of the centroids of ring(I) on plane of ring(II) (Å), Dist.: shorter distances between non-hydrogen atoms of rings (I) and (II). [b] Rings: 1A: N1, C2, C3, C4, C5, C6.

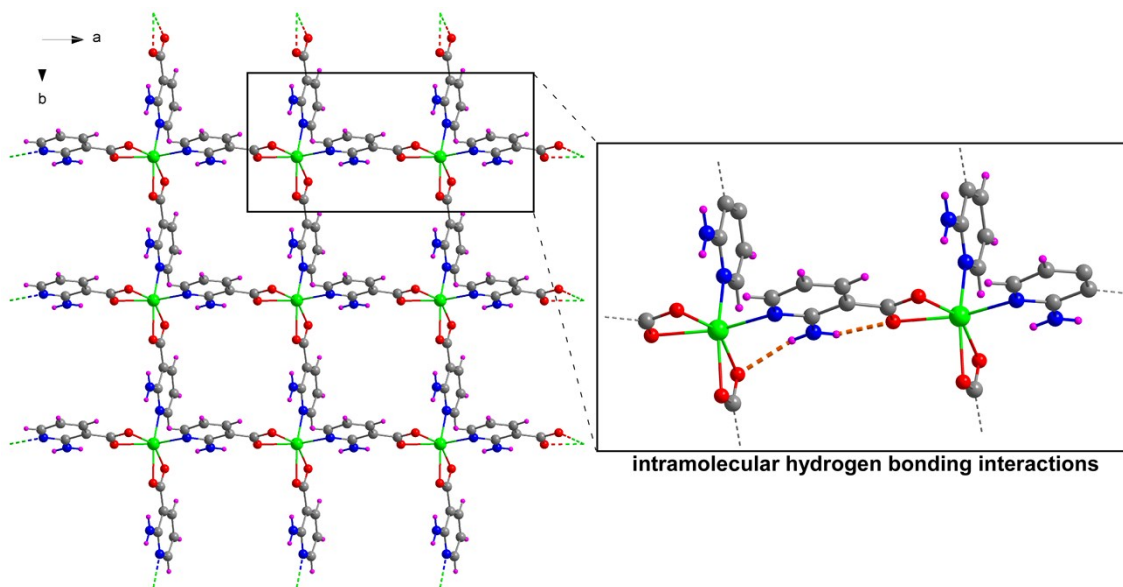


Figure S2. View of the 2D layer of 1 showing π – π interactions between layers along: (a) crystallographic b axis and (b) c axis.

S3. FT-IR spectroscopy.

FTIR spectra of **1** and **2** are almost identical so only that of **1** will be discussed in detail (Figure S3). Main IR active bands of **1** have been assigned according to bibliography¹ and the frequency modes derived from a DFT-optimized model of the compound (see Figure S13). At high frequencies, spectrum of **1** shows two intense bands at 3400 and 3250 cm^{-1} that correspond to the exocyclic amino group. Between 3100 and 2900 cm^{-1} , some weak shoulders attributed to C–H vibrations of the pyridine ring of the ligand are observed. Many intense bands corresponding to the asymmetric stretching of the carboxylate group in addition to the C–C and C–N bonds of the aromatic ring occur in the 1660–1450 cm^{-1} range, while the symmetric stretching vibrations of the carboxylate groups occur in the lower range of 1400–1200 cm^{-1} . At lower frequencies, the remaining bands are assigned to the distortions originated in the aromatic ring and the carboxylate groups of the 2ani ligand. The vibration bands of the Zn–O and Zn–N bonds are observed around 560–530 cm^{-1} .

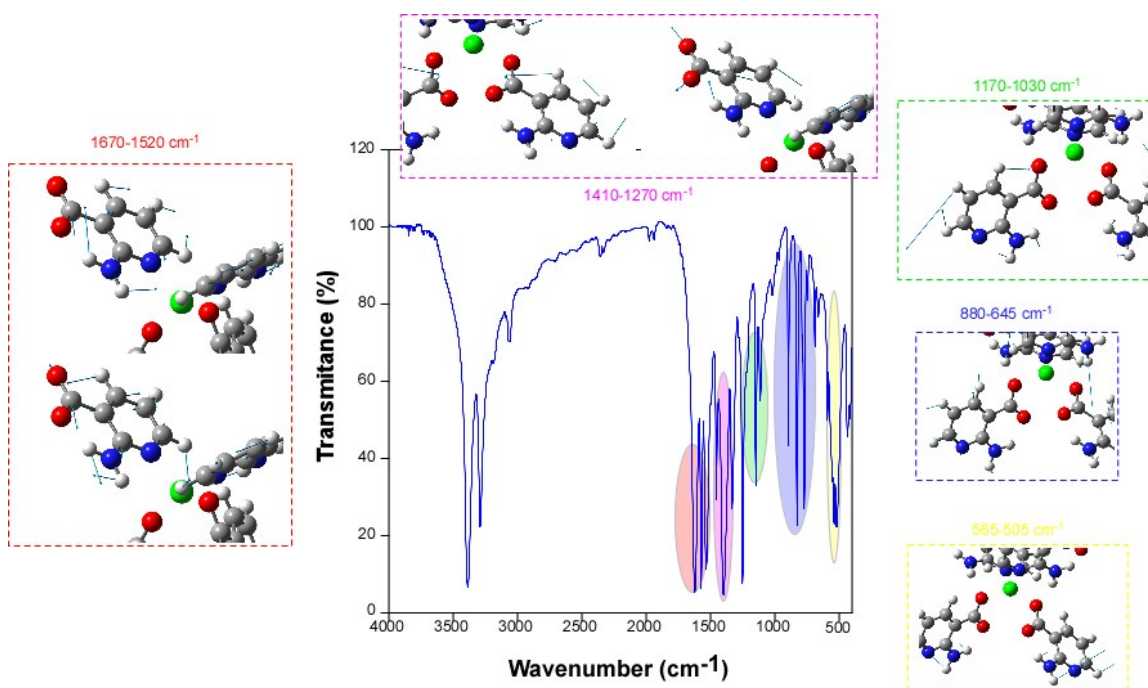


Figure S3. FTIR spectrum of compound **1** together with the normal vibration modes.

¹ Swisicka, R.; Regulska, E.; Samsonowicz, M.; Lewandowski, W. *Polyhedron*, 2009, **28**, 3556.

S4. Thermogravimetric results for compound 2.

Compound 2 shows a similar thermogravimetric behaviour compared to that of 1. The TG curve exhibits a plateau between room temperature and 400 °C, which confirms the absence of crystallization solvent molecules in the crystal structure. Upon heating, this compound decomposes by exhibiting two strong exothermic peaks at 425 and 460 °C, in such a way that CdO is obtained as final residue above 490 °C (calc. 33.2%; found 32.9%).

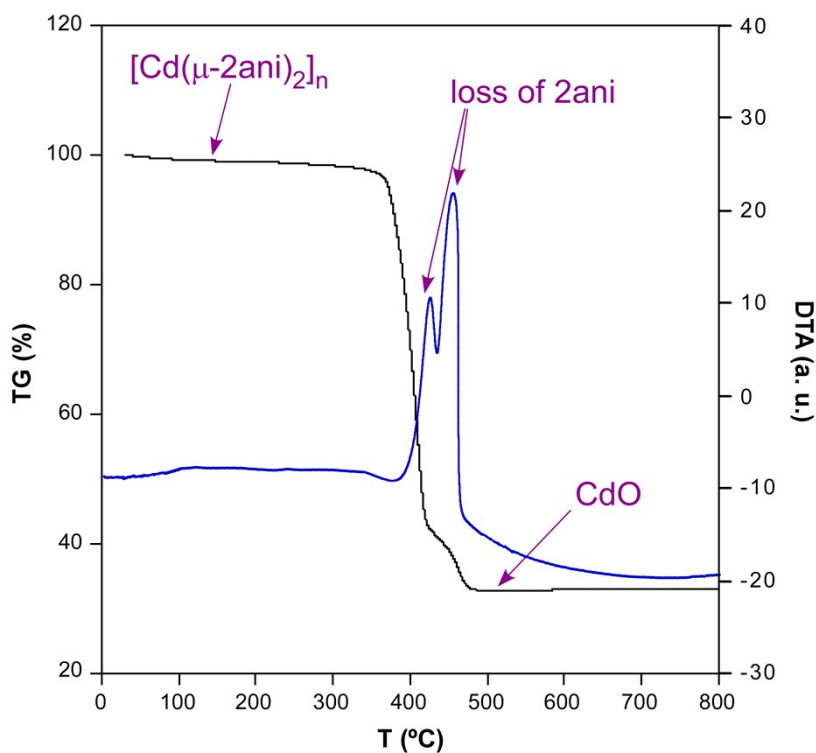
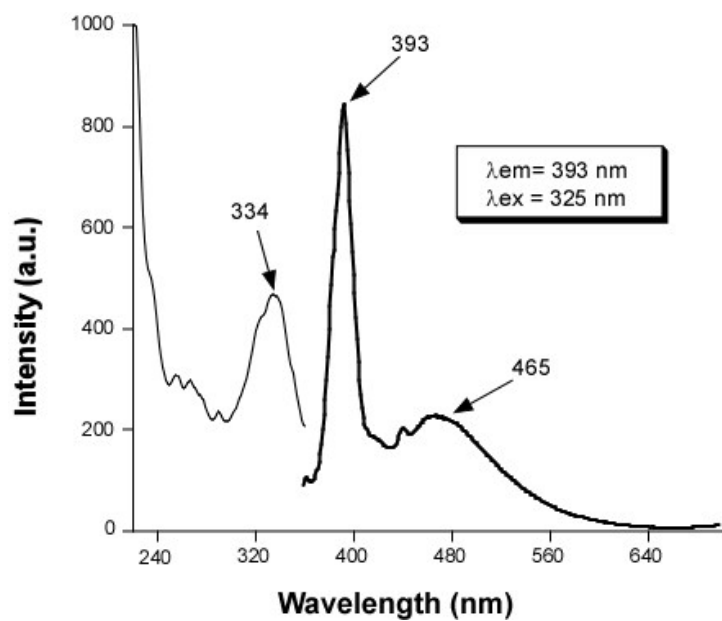
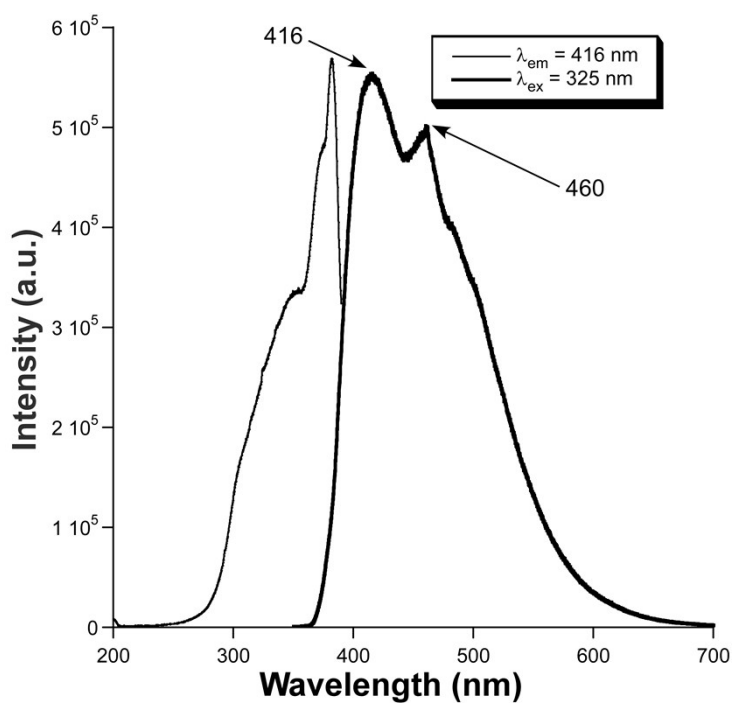


Figure S4. TG (black line) and DTA (blue line) curves for compound 2.

S5. Photoluminescence measurements.



(a)



(b)

Figure S5. Excitation and emission spectra of the H2ani ligand at (a) room temperature (b) 10 K.

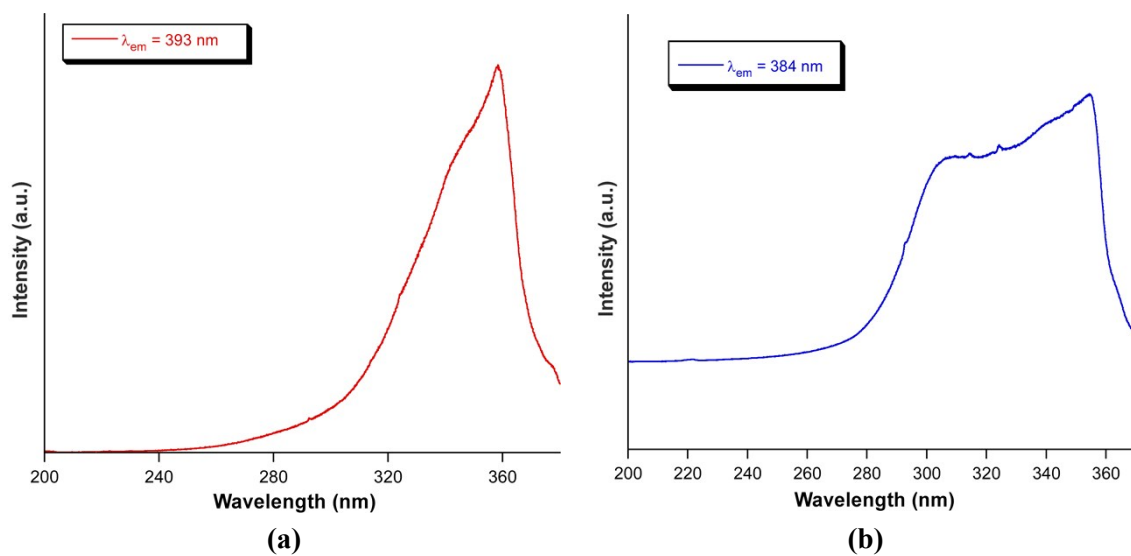


Figure S6. Excitation spectra of compounds: (a) **1** and (b) **2** at room temperature monitoring their maximum emission wavelength.

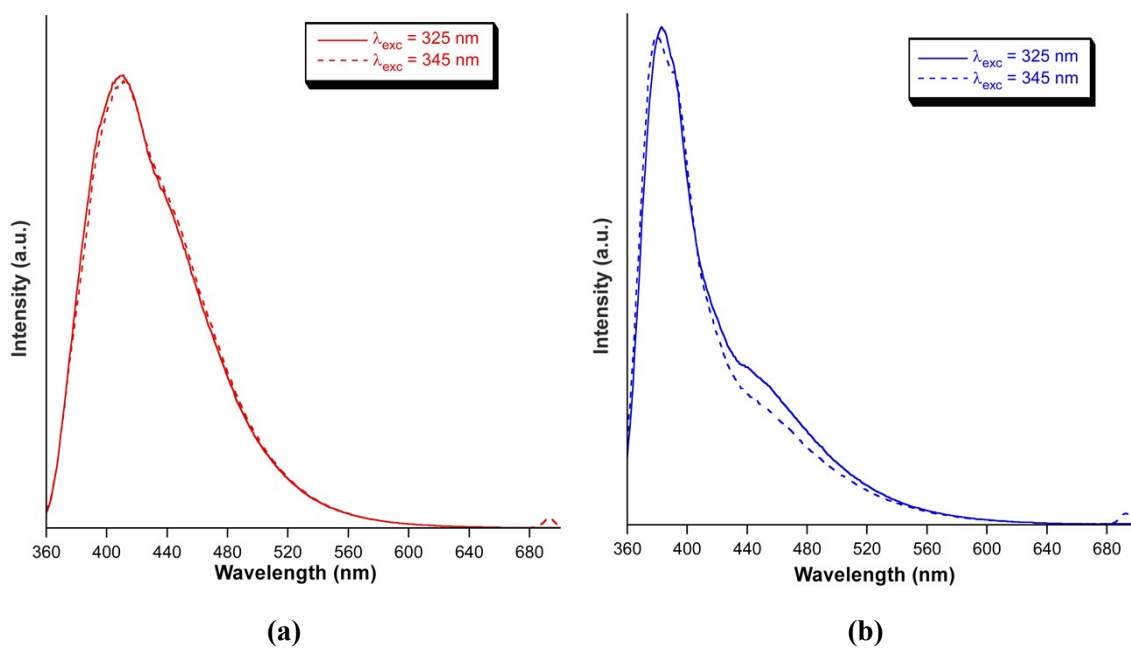


Figure S7. Emission spectra of compounds: (a) **1** and (b) **2** at room temperature excited with different wavelengths.

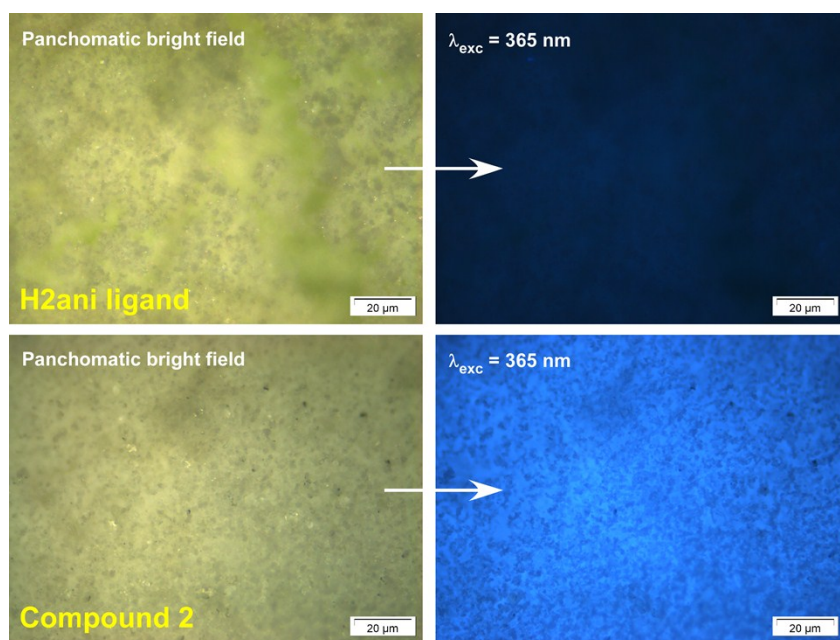


Figure S8. Comparative of micro-PL images taken on H2ani ligand and compound 2 under panchromatic field and UV radiation.

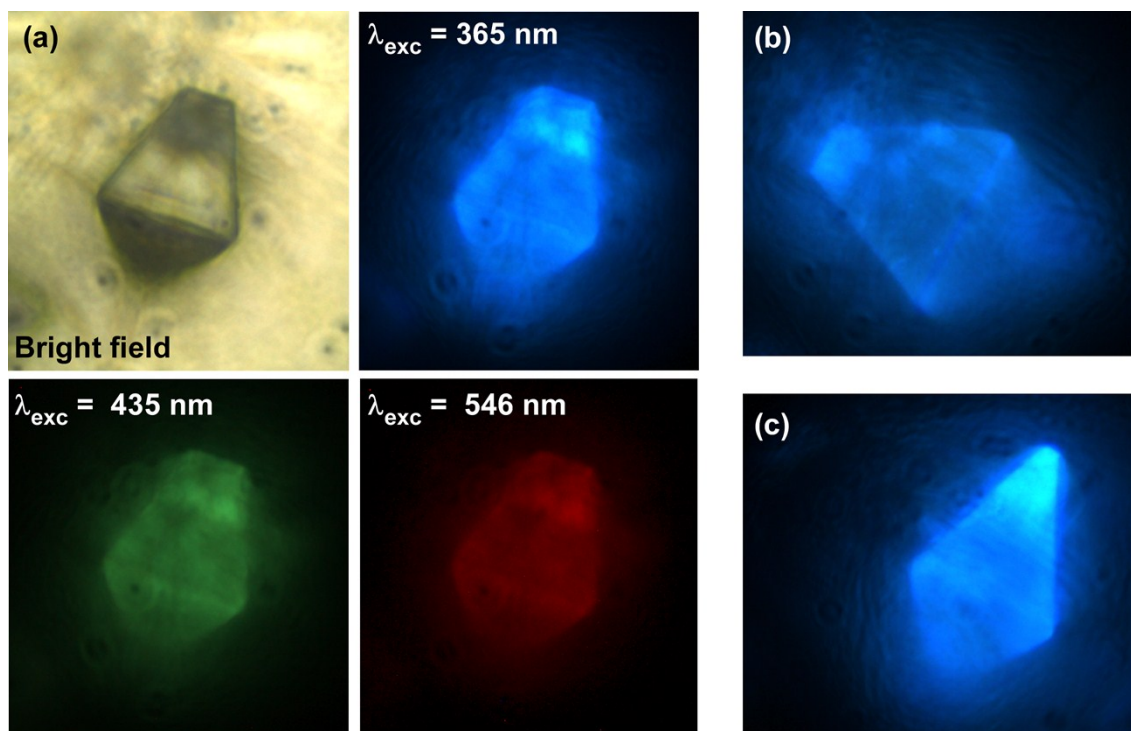


Figure S9. Micro-PL images taken on several crystals of compound 1 under panchromatic field and different excitation wavelengths showing the waveguiding behaviour.

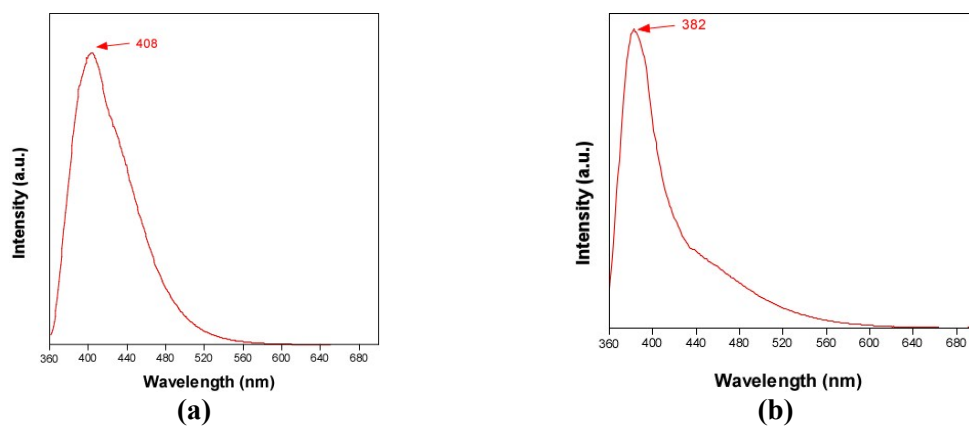
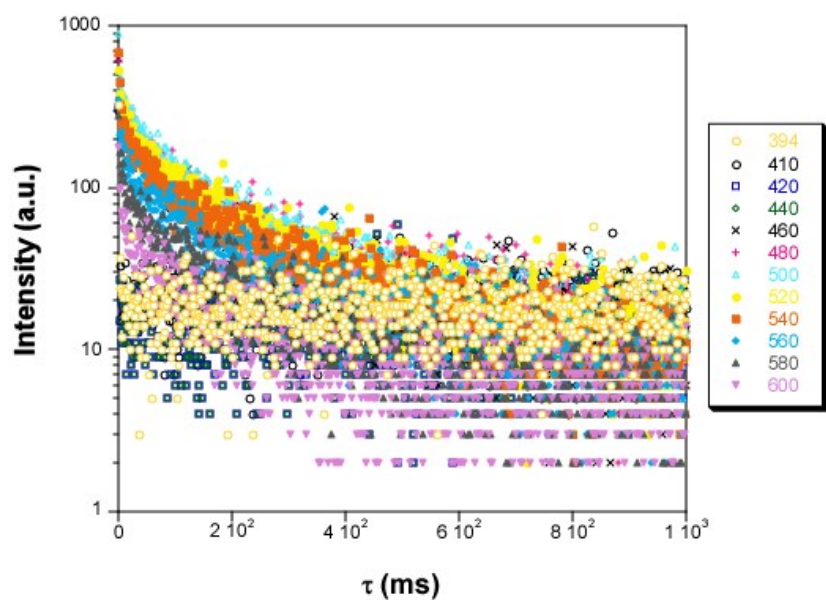


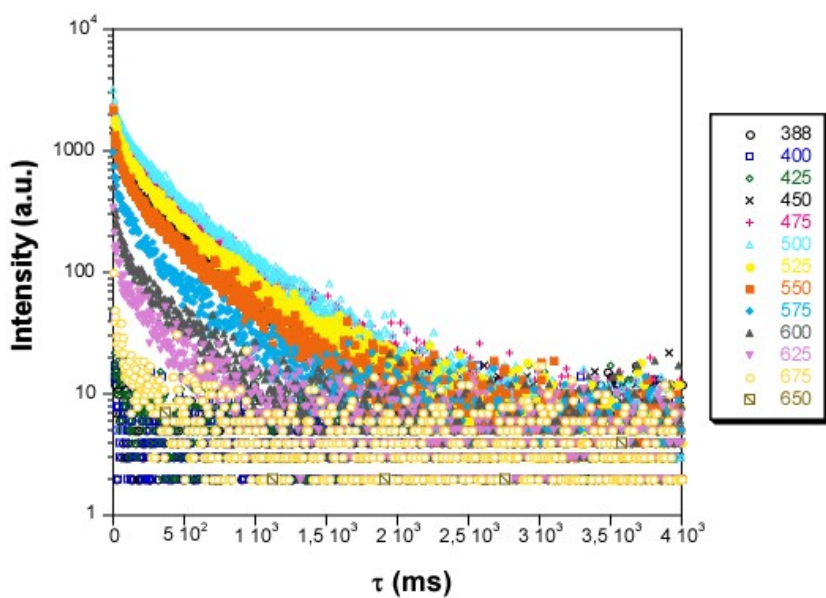
Figure S10. Emission spectra under excitation at 325 nm of compounds: **(a) 1** and **(b) 2** at room temperature.

S6. Lifetime measurements.

Lifetime measurements were initially performed at 10 K using polycrystalline samples for both compounds **1** and **2** under excitation at 325 nm for some selected emission wavelengths. The decay curves were recorded employing different exposure times in order to achieve 10^4 counts in the pulse of reference. Given the different nature of the emissions (fluorescence and phosphorescence), a microsecond pulse lamp was employed. For compound **1**, several curves were recorded in the fluorescent region and twelve decay curves were measured (one each *ca.* 20 nm) in the 460–600 nm emission range. Instead, the fluorescent signal was only observed in the lower wavelength region for compound **2** (at 385, 400 and 425 nm), whereas thirteen decay plots were recorded (one each *ca.* 25 nm) in the 385–650 nm emission range for compound **2**. The curves were analyzed by tail fitting using two or three lifetimes in order to reproduce fairly the non-linear distribution.

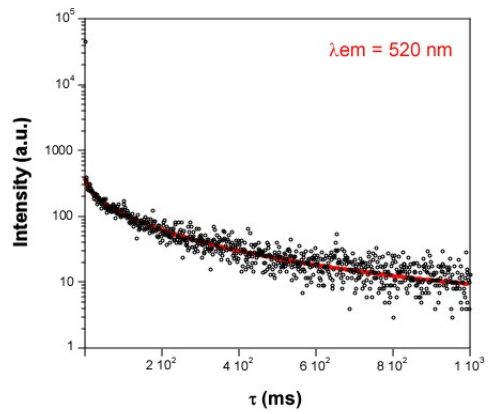
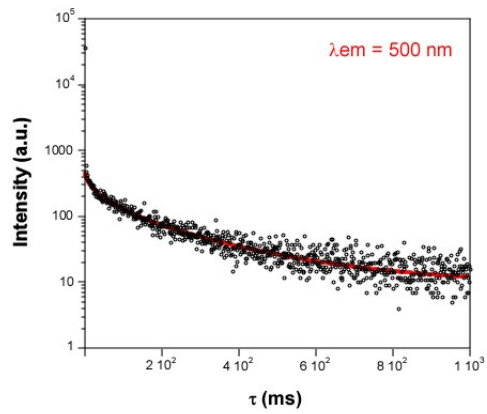
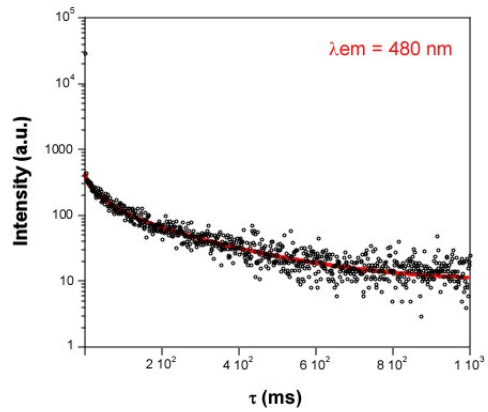
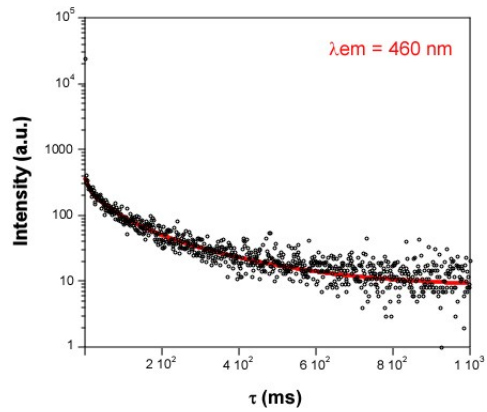
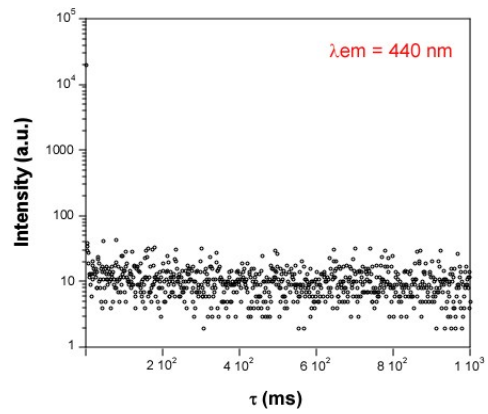
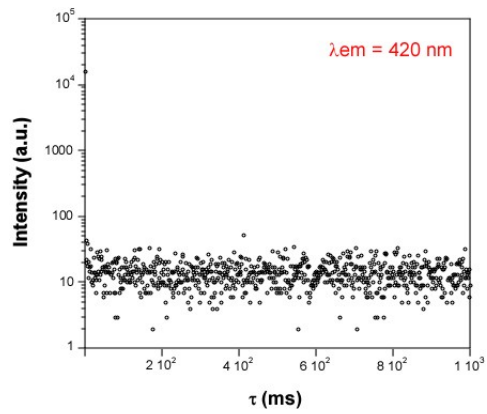
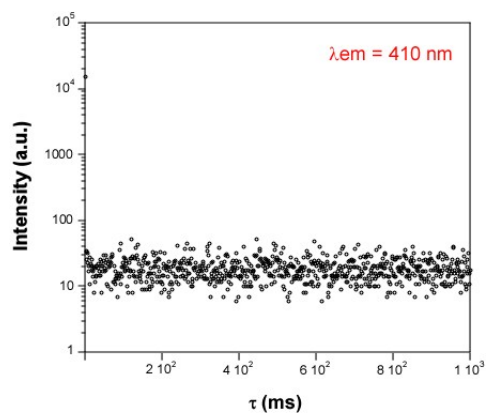
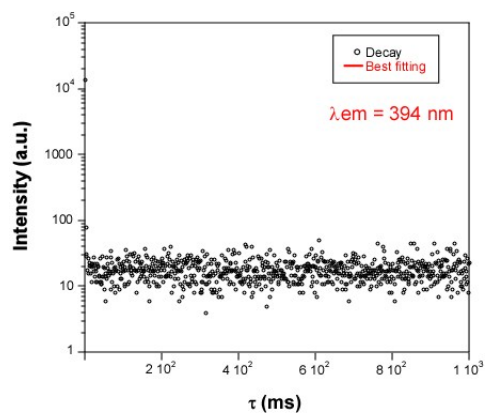


(a)



(b)

Figure S11. Decay curves at selected emission wavelengths upon excitation at 325 nm for (a) 1 and (b) 2.



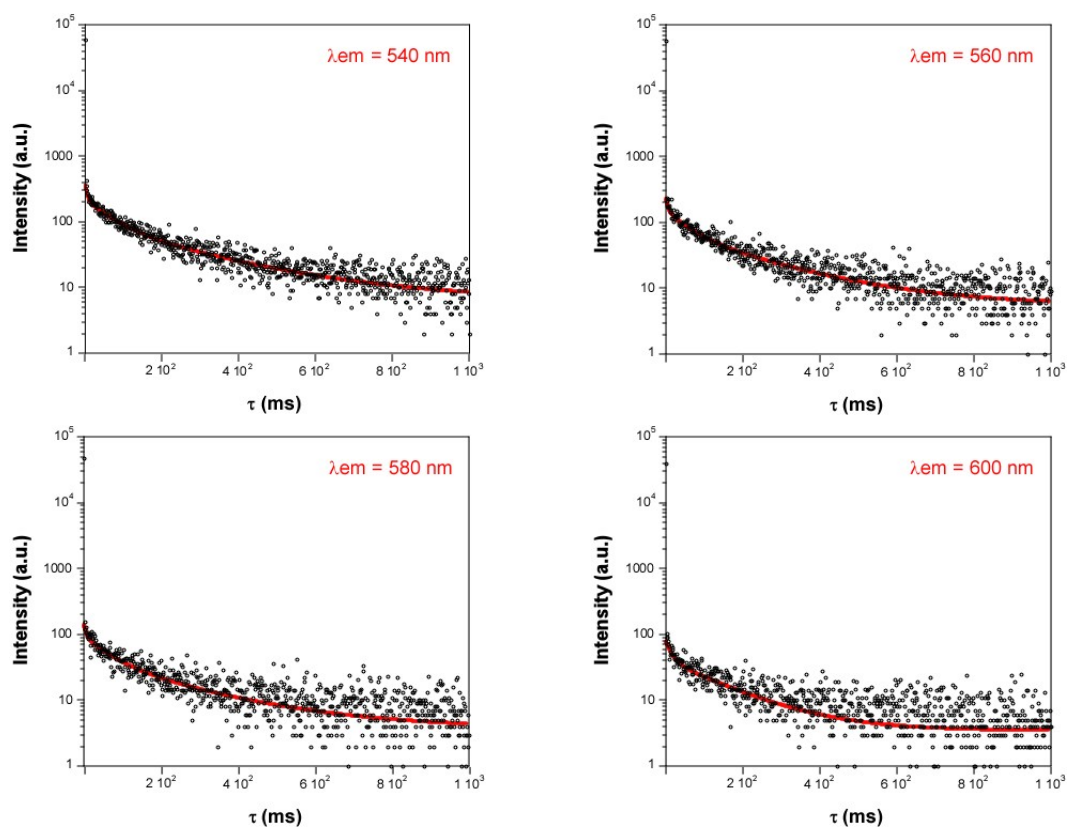


Figure S12. Emission decay curves at selected emission wavelength (every *ca.* 20 nm in the 460–600 nm range) showing the best fitting for **1**.

Table S4. Best fit results of decay curves performed at 10K monitoring different emission wavelengths for **1**.

Wavelength (nm)	τ_1 (ms)	τ_2 (ms)	τ_3 (ms)	Chi Sq.
394	< 0.1	–	–	–
410	< 0.1	–	–	–
420	< 0.1	–	–	–
440	< 0.1	–	–	–
460	10(1) / 4%	61(5) / 31%	215(10) / 65%	1.600
480	7(1) / 2%	48(3) / 22%	227(5) / 75%	1.619
500	9(1) / 3%	65(4) / 25%	245(9) / 71%	1.524
520	11(1) / 4%	82(5) / 32%	321(24) / 64%	1.692
540	5(1) / 2%	62(3) / 26%	266(11) / 71%	1.656
560	6(1) / 2%	55(4) / 23%	228(9) / 74%	1.701
580	7(1) / 3%	60(6) / 26%	242(14) / 72%	1.689
600	15(1) / 9%	151(3) / 91%	–	1.719

Additionally, variable-temperature measurements were performed at 520 nm emission peak (most long-lived emission). As shown in Table S5, the longest lifetime decreases slowly with rising the temperature.

Table S5. Best fit results of decay curves according to the temperature for **1**.

Temp. (K)	τ_1 (ms)	τ_2 (ms)	τ_3 (ms)	Chi Sq.
10	11(1) / 4%	82(5) / 32%	321(24) / 64%	1.692
100	10(1) / 4%	82(2) / 27%	387(5) / 69%	1.530
150	7(1) / 9%	61(2) / 44%	258(5) / 47%	1.535
200	9(1) / 16%	63(1) / 66%	—	1.675
298	< 0.1	—	—	—

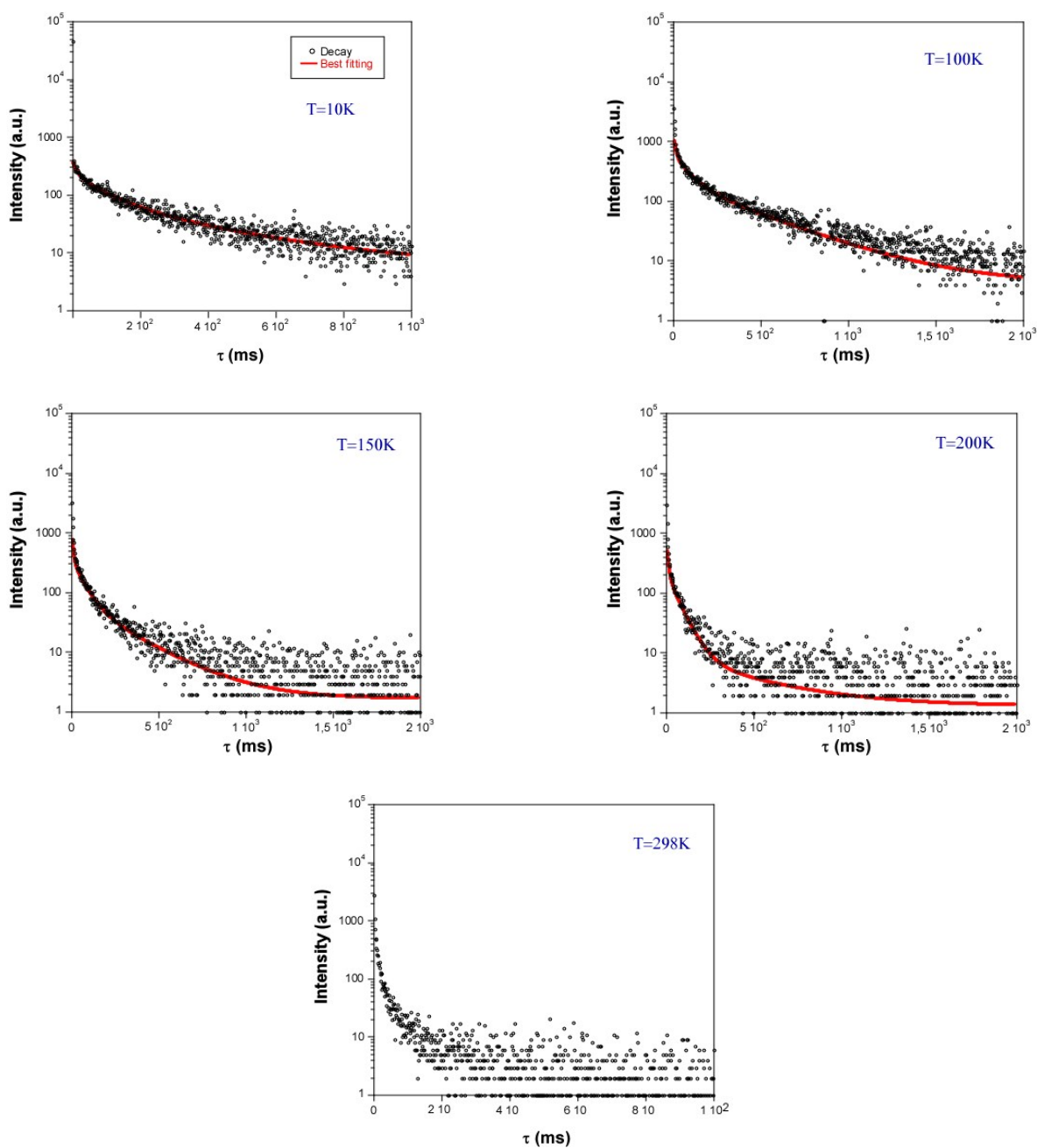
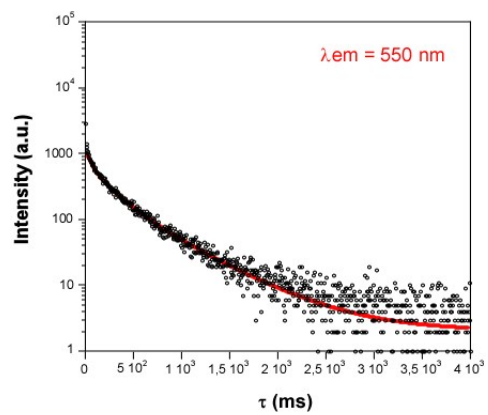
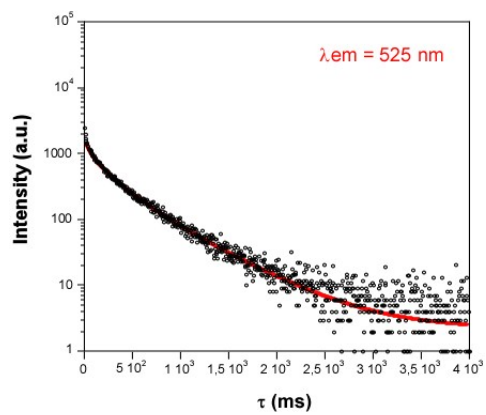
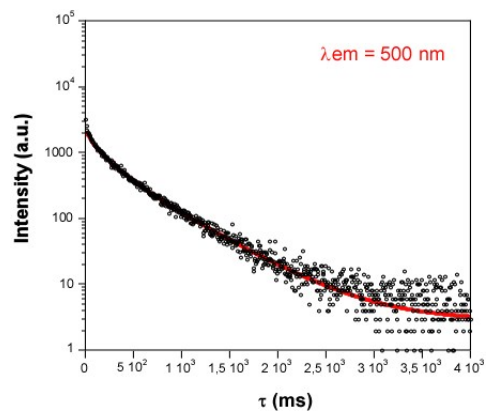
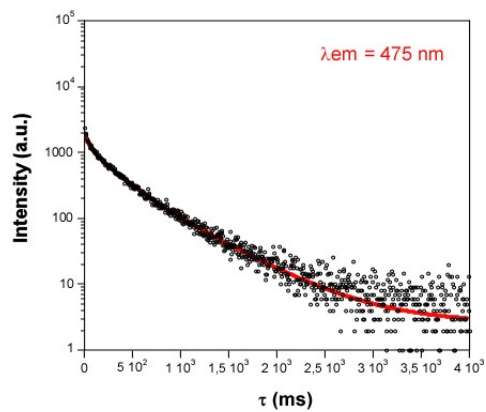
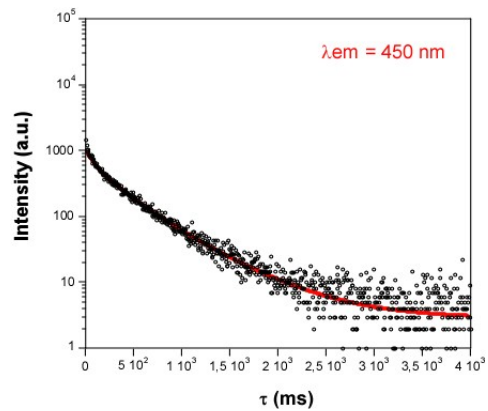
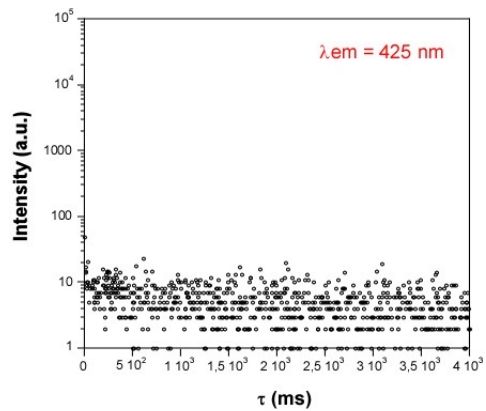
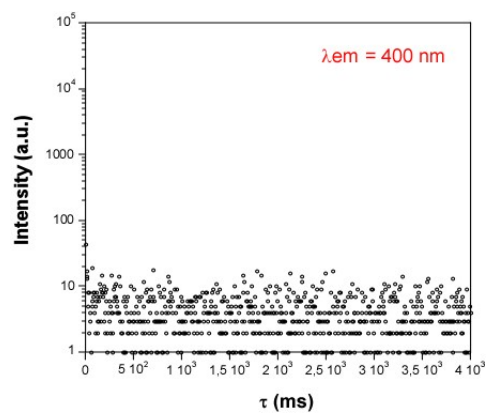
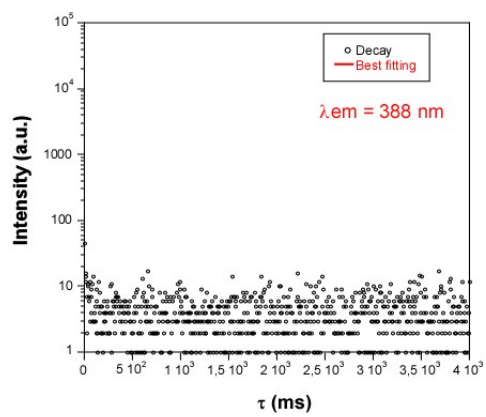


Figure S13. Variable-temperature decay curves fittings at 520 nm emission lines for **1**.



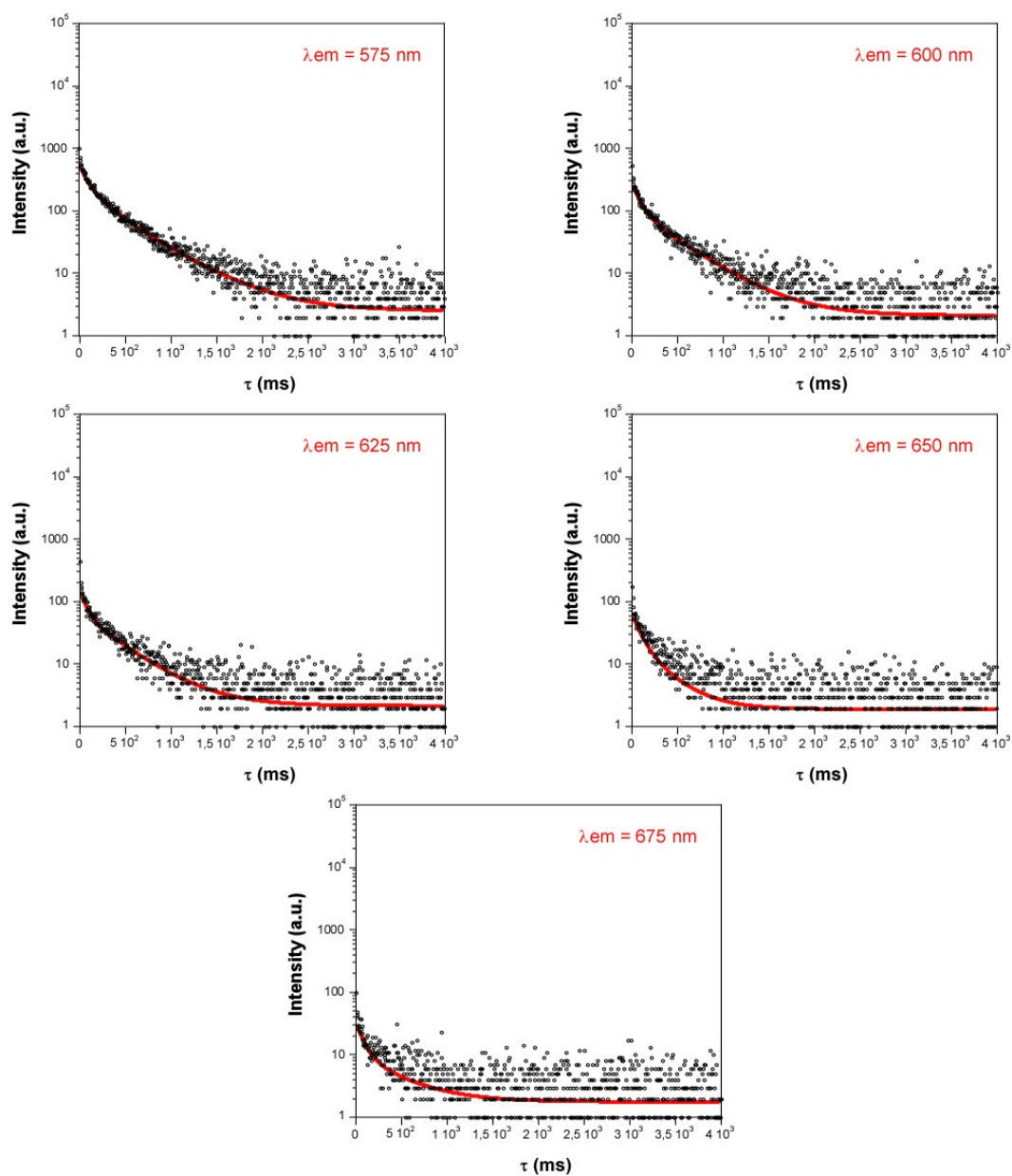
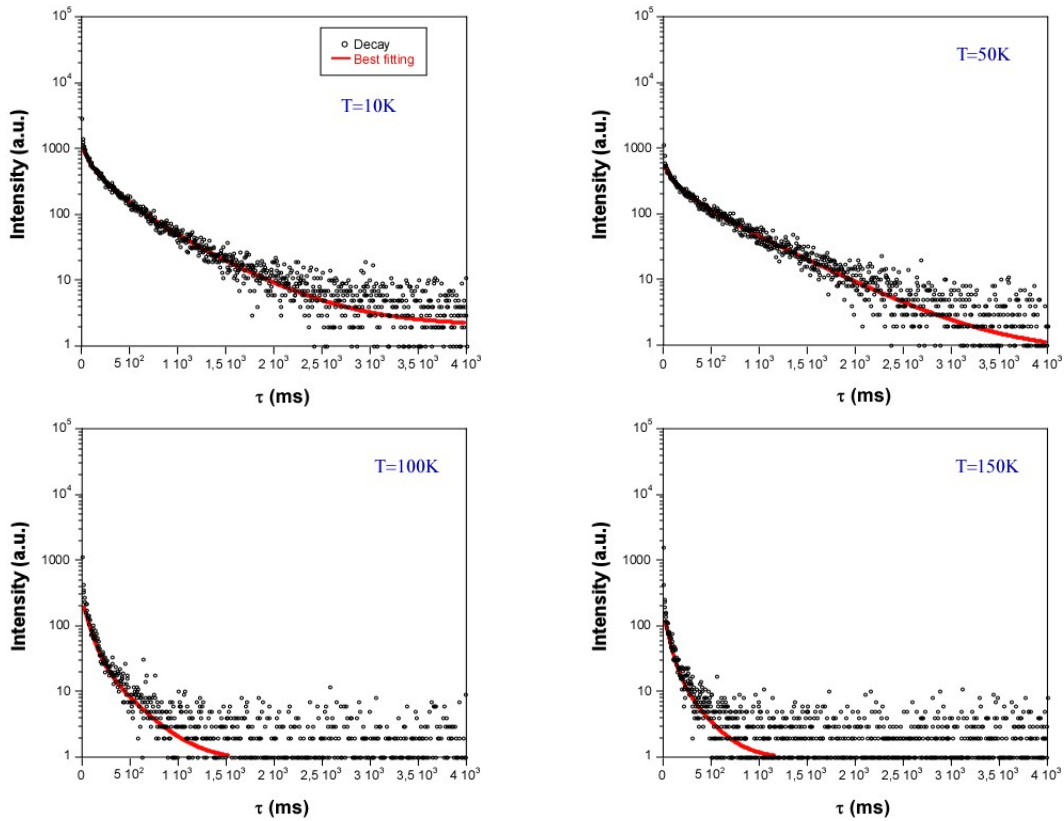


Figure S14. Emission decay curves at selected emission wavelength (every *ca.* 15 nm in the 450–675 nm range) showing the best fitting for **2**.

Table S6. Best fit results of decay curves performed at 10K monitoring different emission wavelengths for **2**.

Wavelength (nm)	τ_1 (ms)	τ_2 (ms)	τ_3 (ms)	Chi Sq.
388	< 0.1	–	–	–
400	< 0.1	–	–	–
425	< 0.1	–	–	–
450	68(7) / 6%	282(24) / 42%	567(28) / 52%	1.674
475	58(6) / 4%	235(12) / 34%	552(10) / 62%	1.875
500	55(5) / 4%	213(10) / 31%	532(7) / 65%	1.722
525	58(5) / 6%	230(12) / 36%	555(11) / 58%	1.770
550	54(4) / 7%	228(14) / 38%	562(15) / 55%	1.774
575	65(15) / 9%	178(35) / 23%	491(12) / 68%	1.832
600	85(4) / 21%	435(6) / 79%	–	1.751
625	71(5) / 17%	403(7) / 83%	–	1.751
650	94(11) / 36%	300(26) / 64%	–	1.863
675	82(9) / 30%	438(36) / 70%	–	1.721

Additionally, variable-temperature measurements were performed at 550 nm emission peak (most long-lived emission). As shown in Table S7, the longest lifetime decreases slowly with rising the temperature.



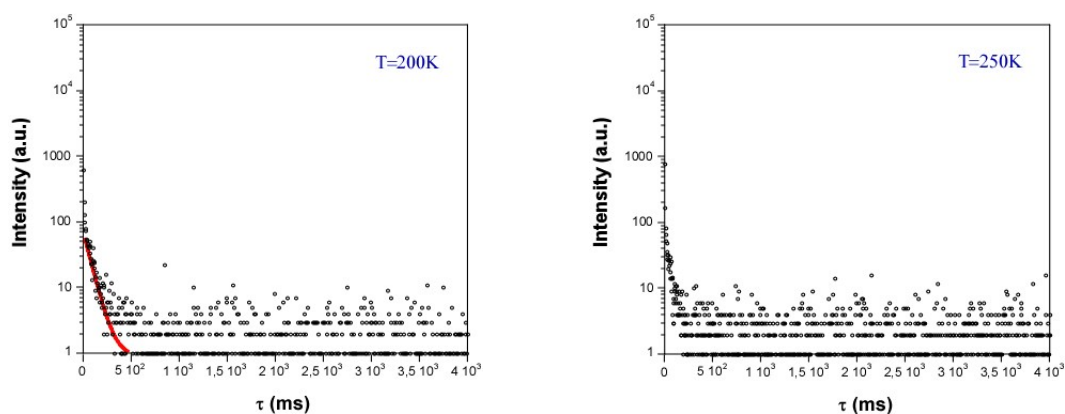


Figure S15. Emission decay curves at 550 nm emission wavelength at different temperatures showing the best fitting for **2**.

Table S7. Best fit results of decay curves according to the temperature for **2**.

Temp. (K)	τ_1 (ms)	τ_2 (ms)	τ_3 (ms)	Chi Sq.
10	54(4) / 7%	228(14) / 38%	562(15) / 55%	1.774
50	54(10) / 4%	193(24) / 18%	609(10) / 78%	1.501
100	70(2) / 49%	276(9) / 51%	—	1.165
150	58(3) / 51%	212(12) / 49%	—	1.140
200	76(2)	—	—	1.058
250	—	—	—	—
300	—	—	—	—

The phosphorescent properties were also measured for H2ani ligand for comparative purposes. While at room temperature it exhibits no phosphorescence, upon cooling to 10 K it shows a sizeable phosphorescence which, compared to that exhibited by compounds **1** and **2**, is weak and short (Figure S16). In good agreement with the results obtained for **1** and **2**, the ligand exhibits very short lifetime in the band maximum ($\lambda_{em} = 416$ nm, see Figure S5b) but remarkably long lifetime in the low-energy tail ($\tau = 97$ ms at $\lambda_{em} = 520$ nm).

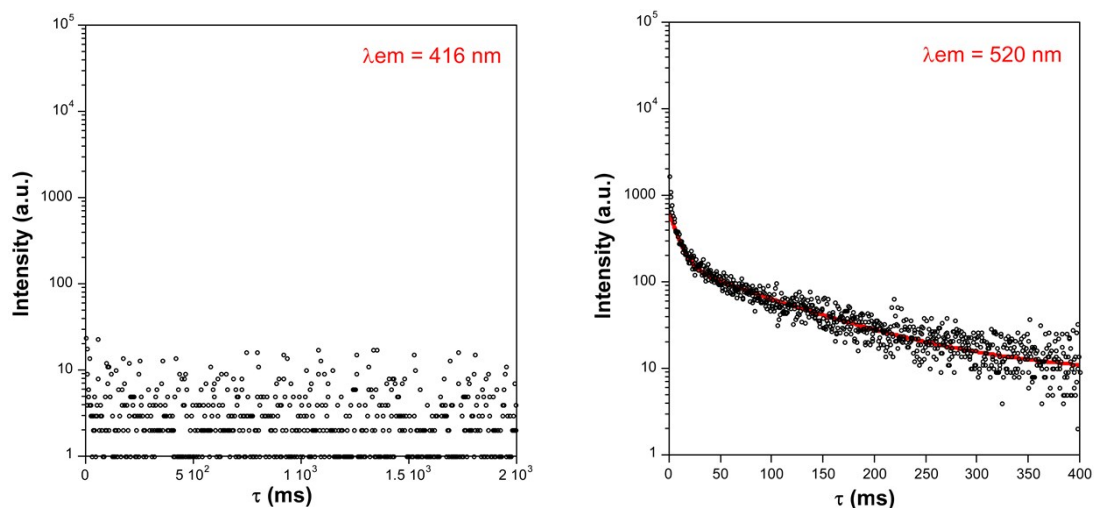


Figure S16. Decay curves of H2ani with $\lambda_{ex} = 325$ nm recorded at (a) $\lambda_{em} = 416$ nm (band maximum) and (b) $\lambda_{em} = 520$ nm (low-energy tail).

S7. TD-DFT computational details.

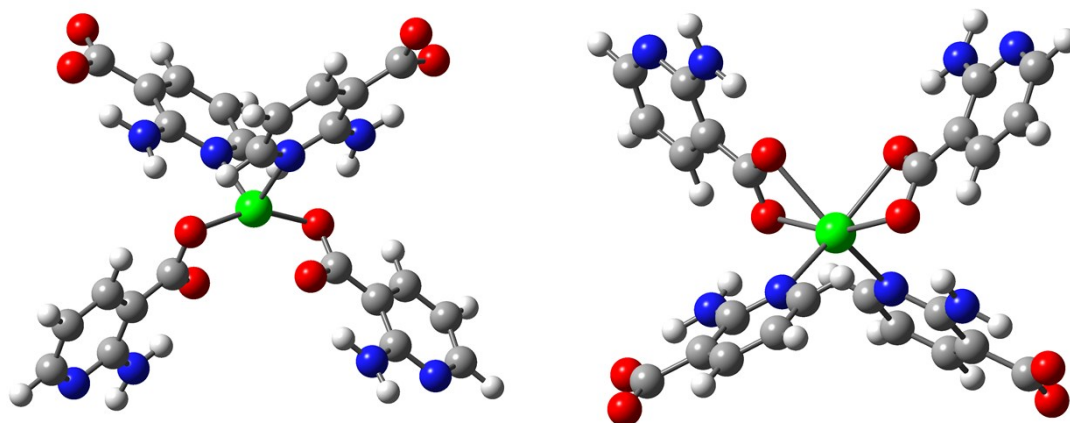
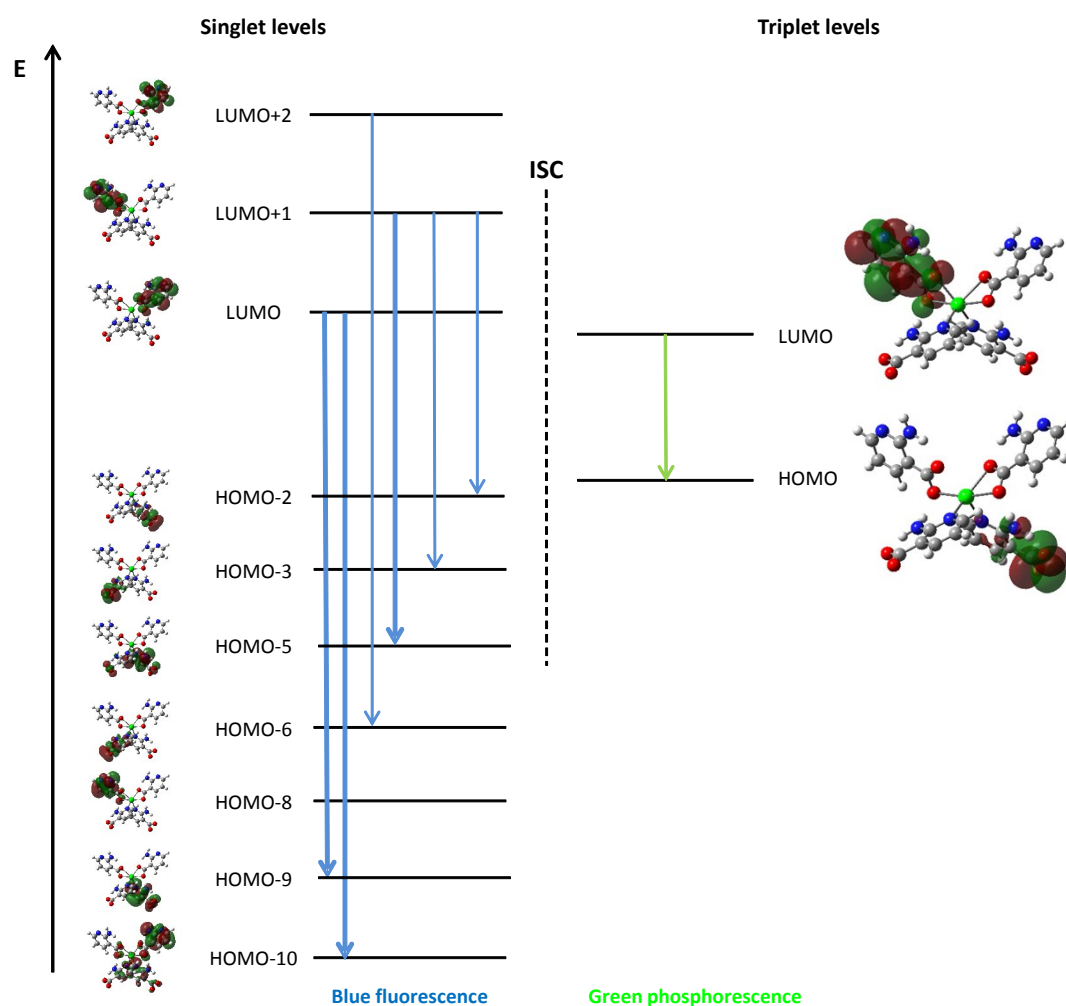


Figure S17. Molecular representation of models **1** and **2** used for the calculations.



Scheme S1. Energy diagram of the orbitals involved in the electronic transitions resulting in fluorescent (left) and phosphorescent (right) emissions of model **2**. ISC: Intersystem crossing.

Table S8. Calculated main excitation energies (nm), singlet electronic transitions and associated oscillator strengths of model **1** in gas phase.

Exp. λ (nm)	Calcd. λ (nm)	Significant contributions	Osc. strength (a.u.)
330	300	HOMO - 9 \rightarrow LUMO (45%)	0.118
		HOMO - 8 \rightarrow LUMO + 1 (42%)	
		HOMO - 3 \rightarrow LUMO + 4 (3%)	
	302	HOMO - 9 \rightarrow LUMO + 1 (45%)	0.122
	HOMO - 8 \rightarrow LUMO (50%)		

Table S9. Calculated main excitation energies (nm), singlet electronic transitions and associated oscillator strengths of model **2** in gas phase.

Exp. λ (nm)	Calcd. λ (nm)	Significant contributions	Osc. strength (a.u.)
333	305	HOMO - 9 \rightarrow LUMO (51%)	0.182
		HOMO - 8 \rightarrow LUMO + 1 (41%)	
	307	HOMO - 9 \rightarrow LUMO + 1 (41%)	0.145
		HOMO - 8 \rightarrow LUMO (51%)	
		HOMO - 1 \rightarrow LUMO + 4 (2%)	

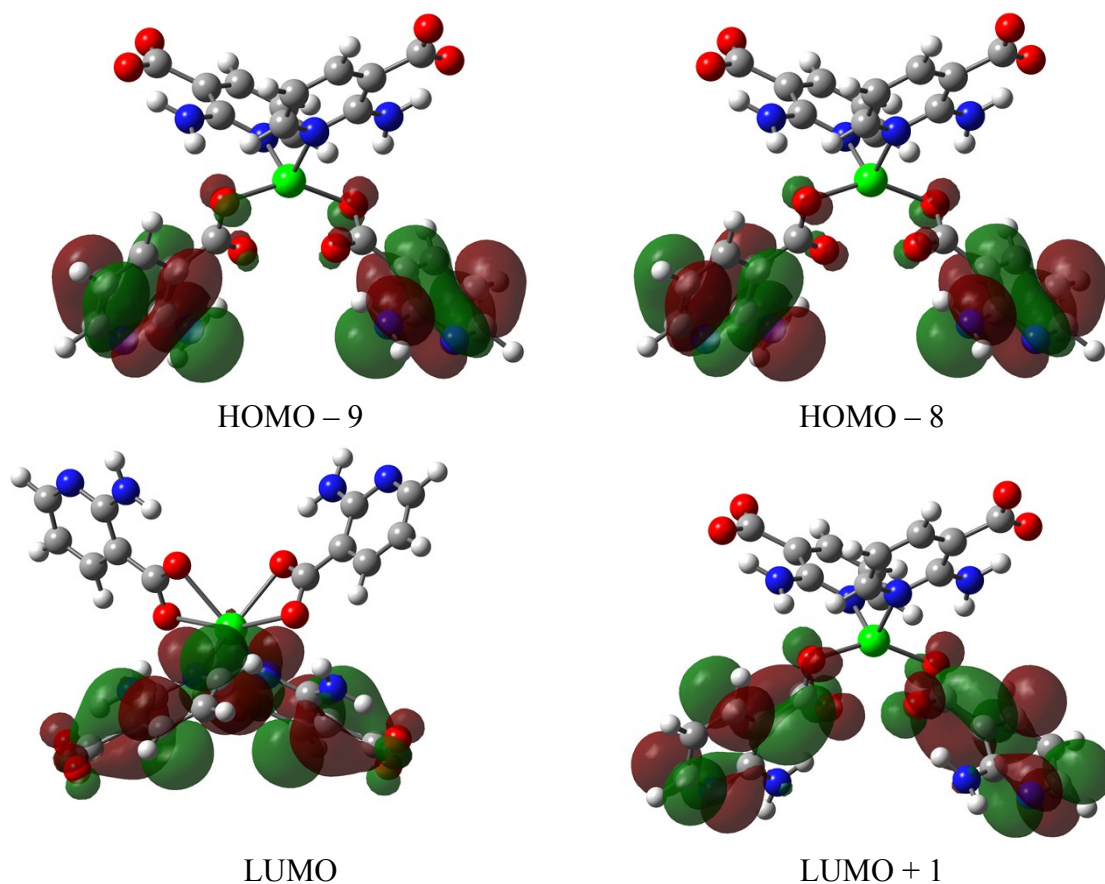


Figure S18. Highest Occupied and Lowest Unoccupied Molecular Orbitals of model **1** involved in the singlet excitation charge transitions.

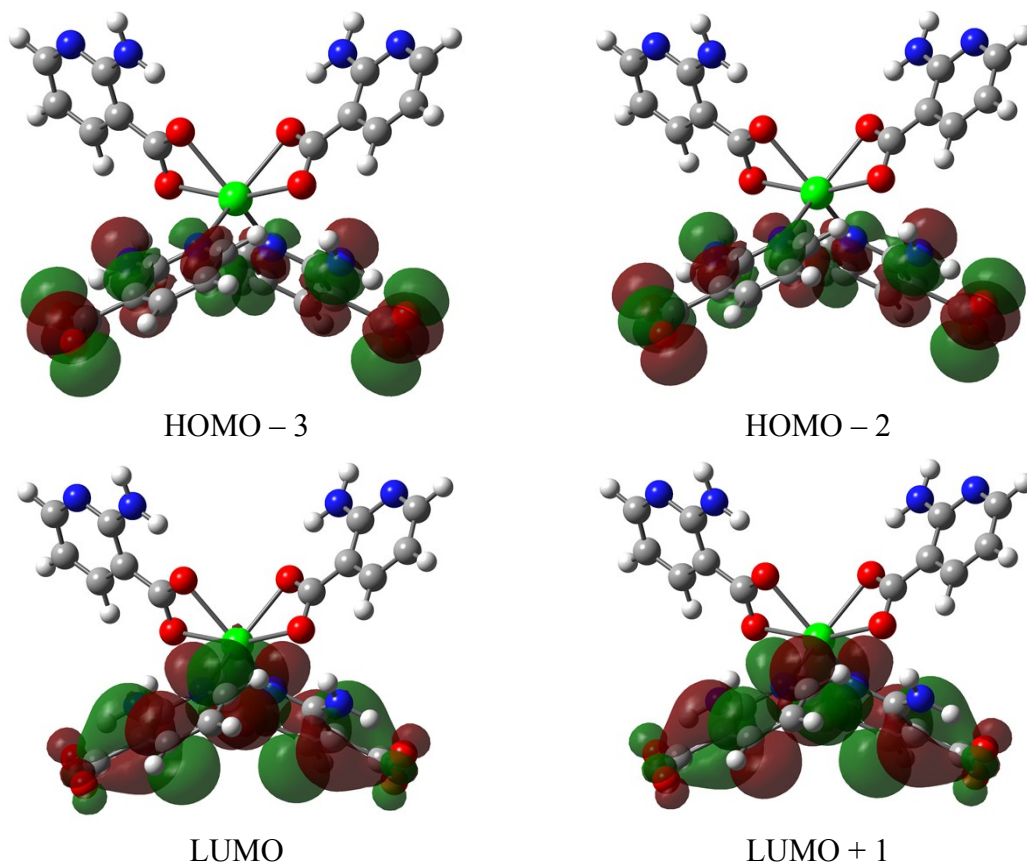


Figure S19. Highest Occupied and Lowest Unoccupied Molecular Orbitals of model 2 involved in the singlet excitation charge transitions.

S8. Calculation of the lowest-lying triplet state (T_1).

The T_1-S_0 energy difference, which corresponds to the main phosphorescent emission line, has been estimated from vertical excitation performed for the optimised geometry of the lowest lying excited triplet state (T_1). The triplet state geometry optimisation and frequencies calculation was performed on a suitable models **1** and **2** (Figure S16) by Gaussian 09 package, using the Becke three parameter hybrid functional with the non-local correlation functional of Lee-Yang-Parr (B3LYP) with the 6-311G++(d,p) basis set for all non-metal atoms and the LANL2DZ basis set along with the corresponding effective core potential (ECP) for the central metal cation.

S9. Time-resolved emission spectra.

TRES measurement was performed for the whole emission spectrum with a step size of 10 nm in the 400–650 nm range given the low emission of the material out of this range. The experiment was performed using a 0.5 Hz of frequency at the pulsed lamp, fixing the excitation band pass at 5 nm and the emission band pass at 2.5 nm. Each spectrum has been deconvoluted according to the standard colour system and plotted in the chromaticity CIE 1931 diagram.

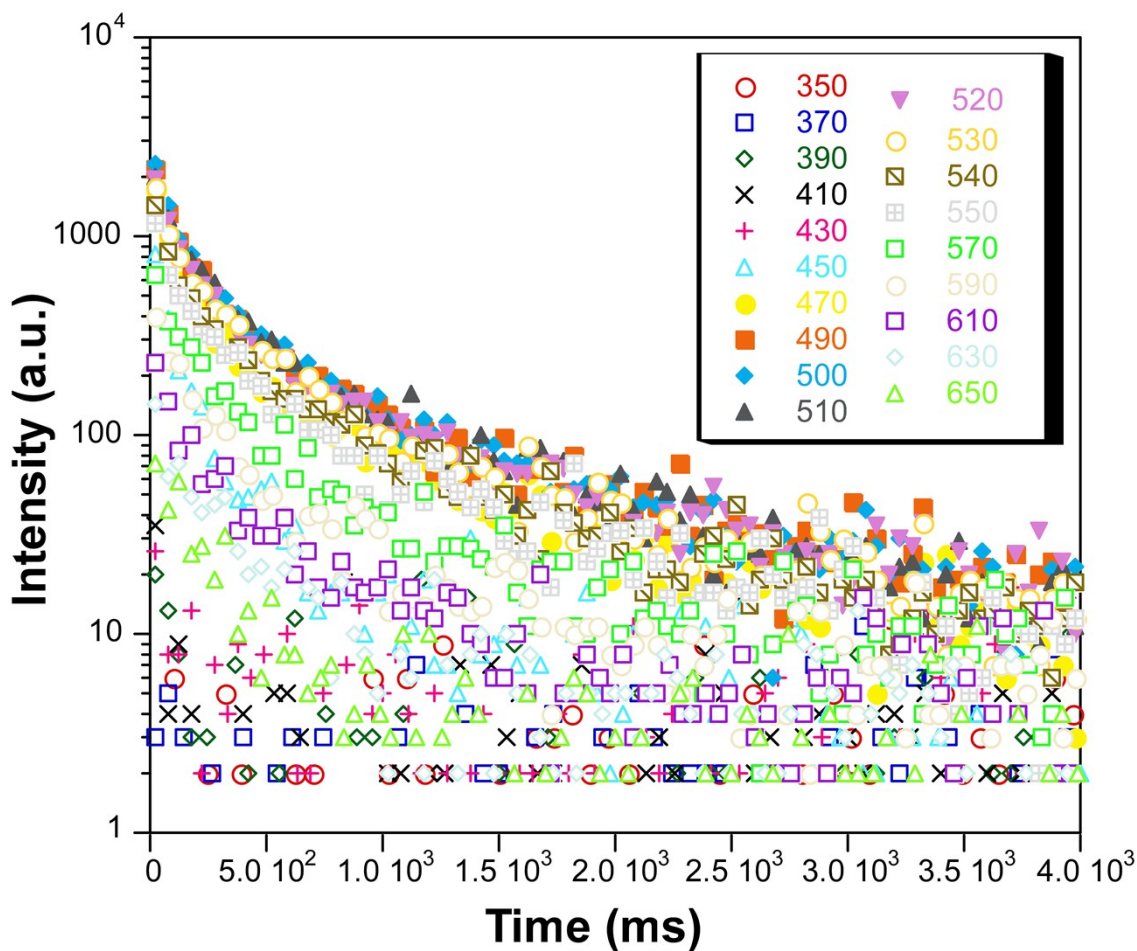


Figure S20. Time-resolved emission spectra in the 350–650 nm region for 1.

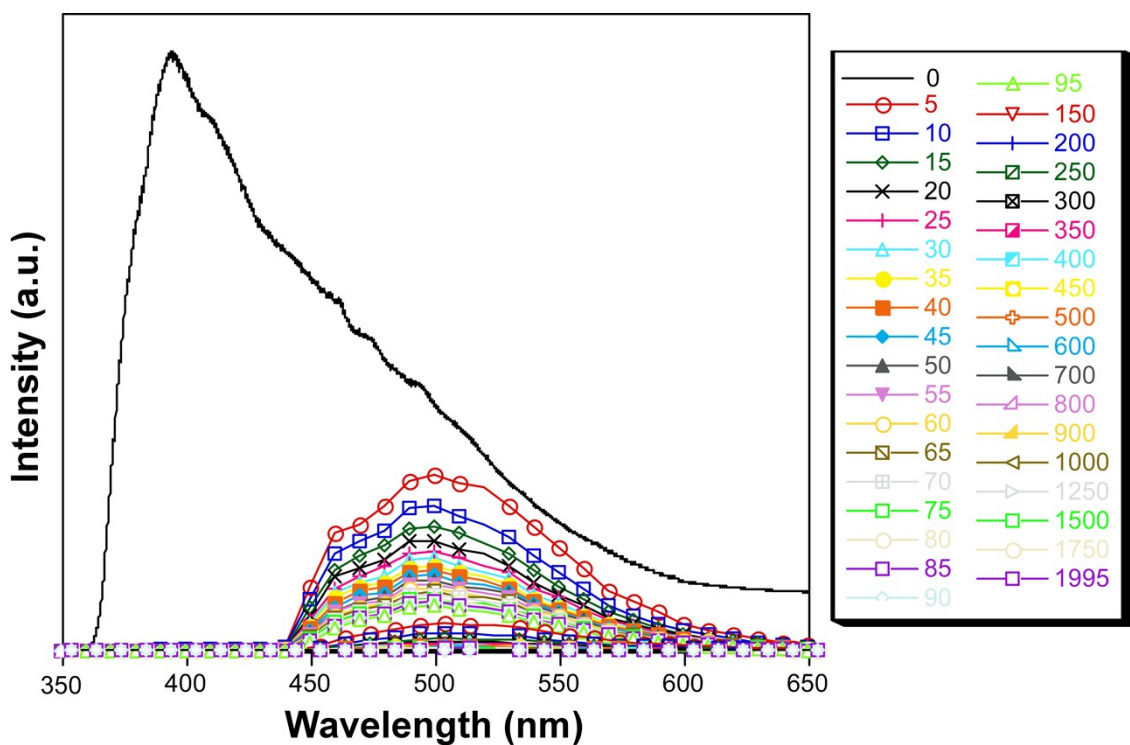


Figure S21. Time-resolved emission spectra at 10 K of **1** at different delays ($\lambda_{\text{ex}} = 333$ nm).

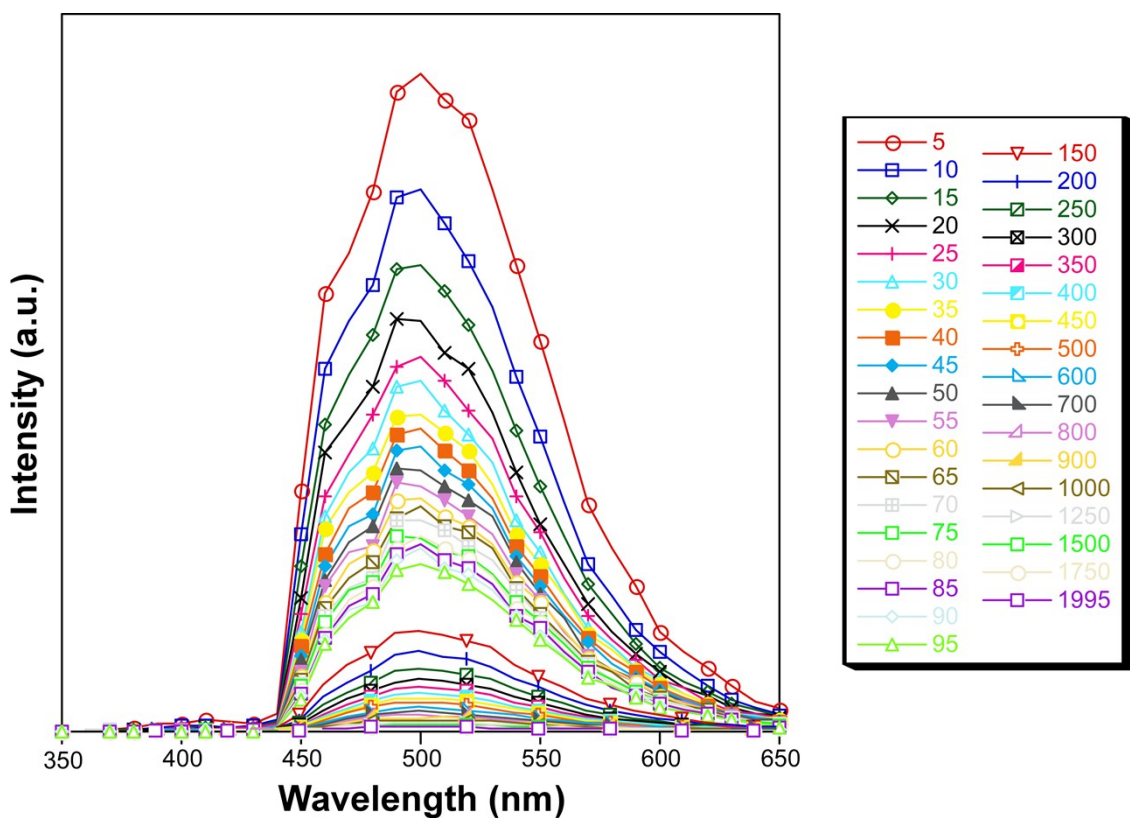


Figure S22. Detailed time-resolved emission spectra at 10 K of **1** at different delays ($\lambda_{\text{ex}} = 333$ nm).

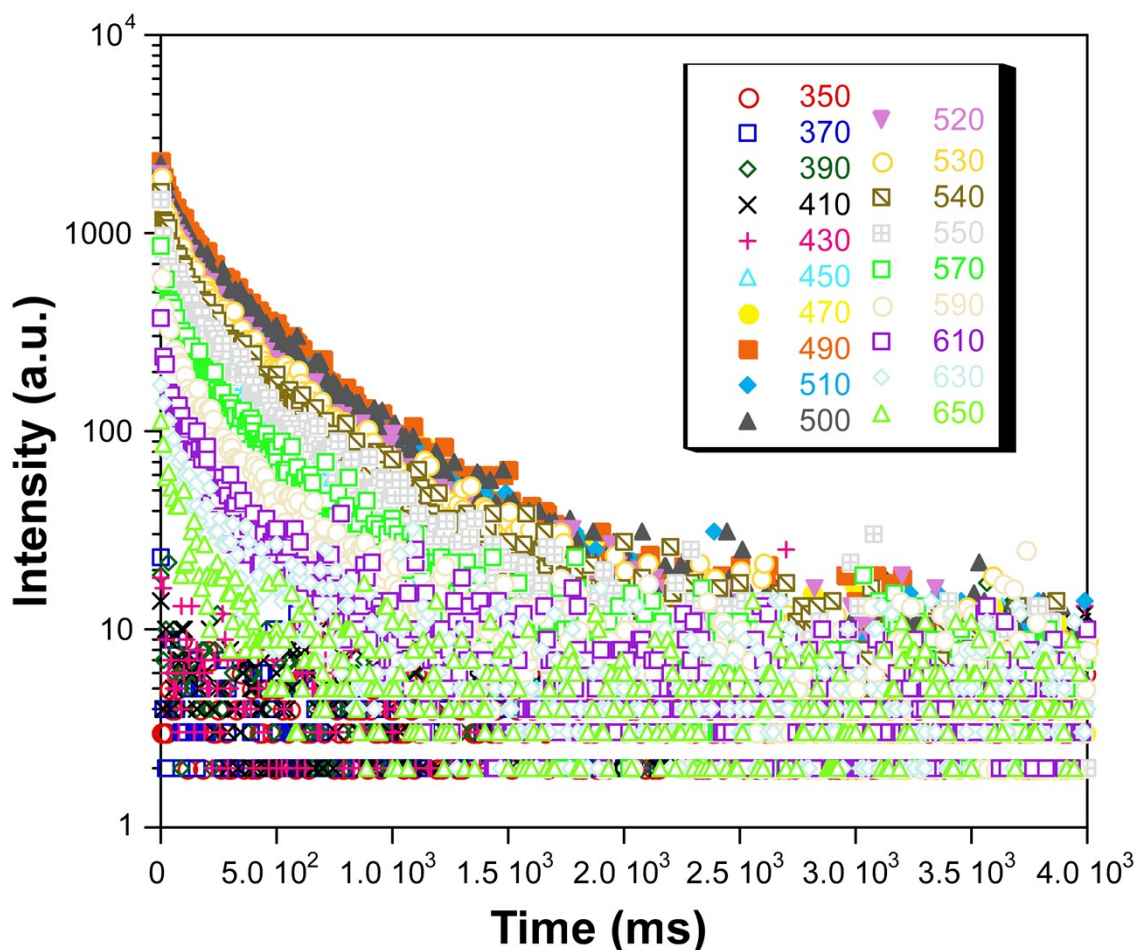


Figure S23. Time-resolved emission spectra in the 350–650 nm region for **2**.

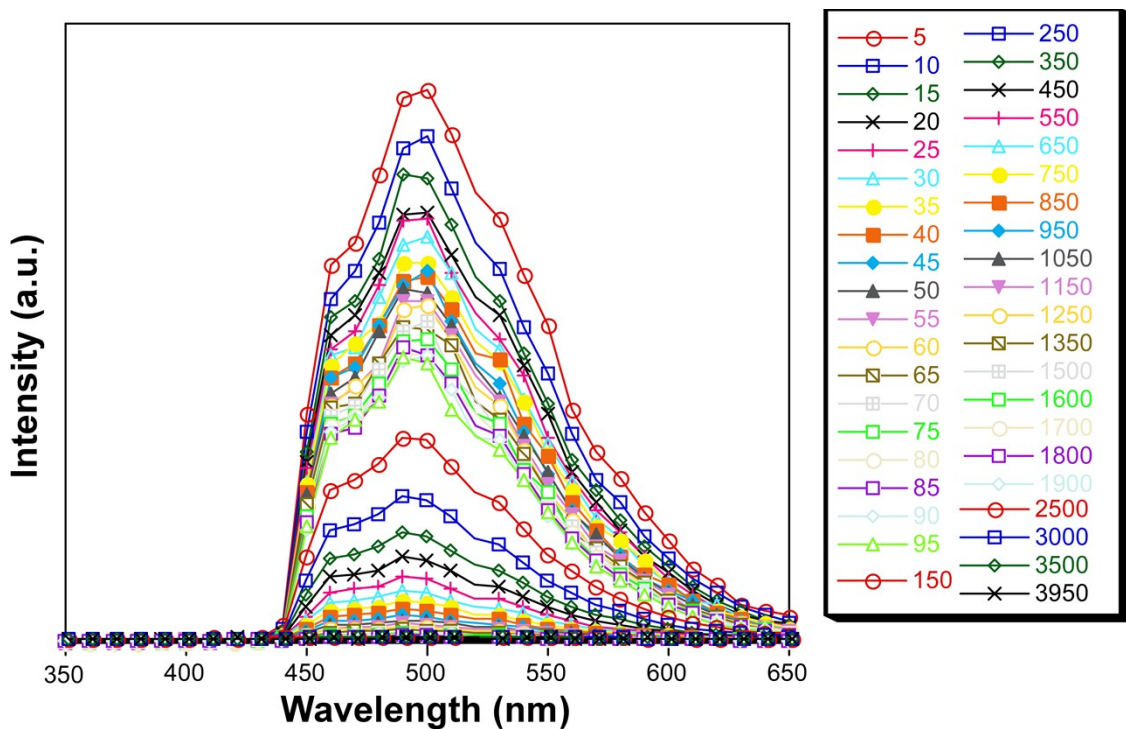


Figure S24. Detailed time-resolved emission spectra at 10 K of **2** at different delays ($\lambda_{\text{ex}} = 333$ nm).